國立臺灣大學理學院物理所
碩士論文

Department or Graduate Institute of Physics

College of Science

National Taiwan University

Master Thesis

以蒙地卡羅法研討 B 介子至質子 Λ 重子衰變

Monte Carlo Study of $B^+ \to p\bar{\Lambda}(1520)$ Decay at Belle

林冠伯
Kuan-Po Lin

指導教授: 王名儒 博士
Advisor: Min-Zu Wang, Ph.D.

中華民國 106 年 2 月
February 2017

國立臺灣大學碩士學位論文
口試委員會審定書

以蒙地卡羅法研討 B 介子至質子 Λ 重子衰變

Monte Carlo Study of $B^+ \to p\bar{\Lambda}(1520)$ Decay at Belle

本論文係林冠伯君（R02222014）在國立臺灣大學物理學系、所完成之碩士學位論文，於民國 105 年 7 月 25 日承下列考試委員審查通過及口試及格，特此證明

口試委員：

_____ （簽名）

（指導教授）

_____　_____

_____　_____

_____　_____

_____　_____

Acknowledgements

In this long long journey,
sometimes it's sunny, but other times stormy.
What beat me but didn't defeat me
have made me stronger, physically and mentally.

In this long long journey,
I walk along, with all your company.
Please accept my sincere gratitude,
my dearest family, and my bonnie.
Thanks to my enemies, if any,
and those who helped me, yet too many.
I believe beside me
you will always be,
in each of the upcoming
long long journey.

摘要

本篇論文探討 B 介子經由 $B^+ \to p\overline{\Lambda}_{1520} \to p\bar{p}K^+$ 雙重子途徑之衰變。本實驗以蒙地卡羅法模擬日本高能加速器 B 介子工廠(KEKB)中 Belle 偵測器收集來自 $\Upsilon(4S)$ 共振態衰變的 7 億 7 千萬 $B\overline{B}$ 介子對。本實驗並應用以神經網路演算法為基礎的 NeuroBayes 來提升訊噪比，以估計 $B^+ \to p\overline{\Lambda}_{1520} \to p\bar{p}K^+$ 分支比在 90%信心水準下的上限值為 5.46×10^{-7}。此模擬結果可對 Belle 偵測器真實數據之分支比量測所幫助。相關主題亦值得於新一代 B 介子工廠(SuperKEKB)進行後續研究。

Abstract

$B^+ \to p\bar{\Lambda}_{1520}$ is one of the simplest two-body baryonic B decay modes. We reconstruct $\bar{\Lambda}_{1520}$ from $\bar{p}$ and K^+, then search for the signal $B^+ \to p\bar{\Lambda}_{1520}$ ($\to p\bar{p}K^+$). Simulating the data collected at the $\Upsilon(4S)$ resonance with the Belle detector at KEKB, we use Monte Carlo method to generate 772 million $B\bar{B}$ pairs collider events. After background suppression, we extract the signal from the Monte Carlo generated data and estimate the branching fraction: $\mathcal{B}(B^+ \to p\bar{\Lambda}_{1520}) < 5.46 \times 10^{-7}$ at the 90% confidence level. This study helps measuring the branching fraction of the real data at Belle detector, and further, data at Belle II detector.

Contents

i

List of Figures

List of Tables

Chapter 1

Introduction

1.1 Standard Model

The goal of particle physics is to study the fundamental constituents of matter and their interactions. The Standard Model (SM) is the currently dominant theory of particle physics, formulated as relativistic quantum field theory. In SM, there are 4 families of elementary particles: 6 flavor of spin-1/2 quarks, 6 types of spin-1/2 leptons, 4 spin-1 gauge bosons and Higgs boson (shown in Fig 1.1), with their anti-particles. Besides, the 3 fundamental interactions within particles in SM are the strong interaction, the electromagnetic interaction and the weak interaction, leaving gravitational interaction excluded.

Quarks, including up (u), down (d), charm (c), strange (s), bottom (b), and top (t) quarks, are the particles participating in strong interactions. On the other hand, leptons contain electrons (e), muons (μ), taus (τ) and their corresponding neutrinos ν_e, ν_μ and ν_τ. Each type of the 3 fundamental interactions is described in terms of the exchange of a spin 1 gauge boson. Gluons (g) mediate the strong interaction, while $W^\pm$ and Z^0 mediate the weak interaction. For all charged particles (quarks are fractional charged, whereas others are integral), they are involved in the electromagnetic interaction, mediated by photons (γ). Finally, Higgs boson (H) is a spin-0 particle, postulated to explain the mechanism how elementary particles acquire their mass.

To sum up, a particle couples to a gauge boson only if it carries the charge of the interaction: electrically charged particles couple to γ; color-charged ones couple to g; and all couple to $W^\pm$ and Z^0 due to weak charges. Fig 1.2 shows the diagram of the summary.

Figure 1.1: SM elementary particles classified as 4 kinds [1]
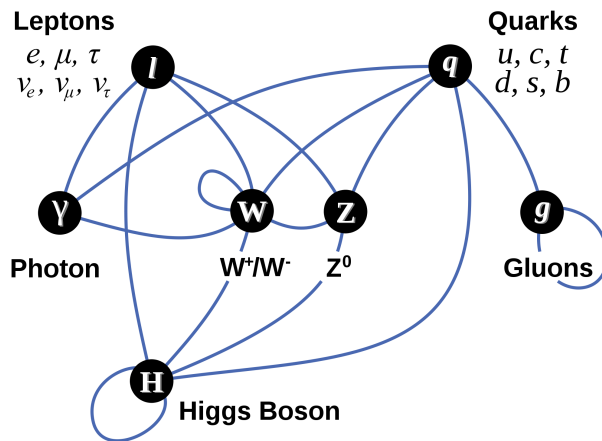
Figure 1.2: Diagram summarizing the interactions between elementary particles

1.1.1 Feynman Diagram

Feynman diagram, invented by Richard Feynman, is not only a graphical representation but also a calculating tool used to evaluate probability of transitions between initial and final states.

A Feynman diagram consists of 3 basic elements: external lines, internal lines and vertices. All Feynman diagrams can be constructed from the Standard Model vertices, partially shown in Fig 1.3. Given the initial and the final states, there are infinite Feynman diagrams associated with it. The diagram with the largest absolute value, the dominant term, is called the lowest-order diagram. However, no matter which order it is, once a Feynman diagram of a transition is drawn, the corresponding QM transition matrix elements can be calculated, applying *Feynman Rules*. Fig 1.4 shows an simple Feynman diagram example.
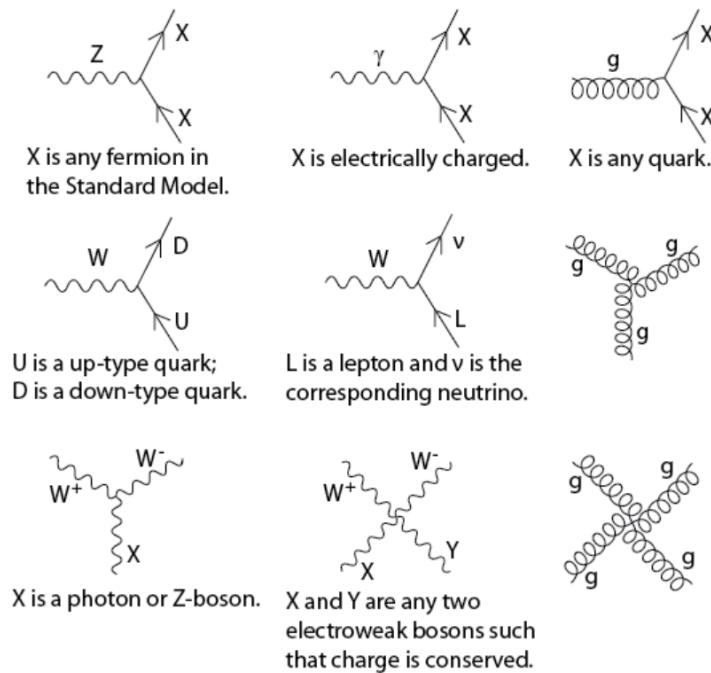
Figure 1.3: The SM vertices
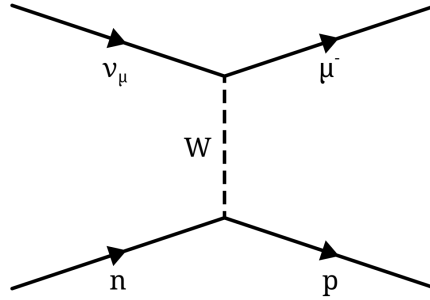
Figure 1.4: A simple Feynman diagram for the neutron decay process: $n \to p\mu^- \bar{\nu}_\mu$.

1.1.2   The Cabibbo-Kobayashi-Maskawa(CKM) matrix

According to SM, leptons or quarks can change their flavor only through weak interactions. Moreover, the weak interaction allows quarks to change from one generation to another. Therefore, the d, s and b quarks are not pure mass eigenstates but mixtures with regard to weak interactions. This concept was proposed by M. Kobayashi and T. Maskawa in 1973 [2] based on Cabibbo mechanism: the mixture eigenstates of d, s and b quark can be represented by a 3×3 unitary matrix called Cabibbo-Kabayashi-Maskawa matrix (CKM matrix).

$$
\begin{pmatrix} d' \\ s' \\ b' \end{pmatrix} = \begin{pmatrix} V_{ud} & V_{us} & V_{ub} \\ V_{cd} & V_{cs} & V_{cb} \\ V_{td} & V_{ts} & V_{tb} \end{pmatrix} \begin{pmatrix} d \\ s \\ b \end{pmatrix} \tag{1.1}
$$

is the form of the CKM matrix.

The entries can be parameterized by 3 mixing angles and 1 CP-violating phase as following, [3]

$$
\begin{pmatrix} c_{12}c_{13} & s_{12}c_{13} & s_{13}e^{-i\delta} \\ -s_{12}c_{23} - c_{12}s_{23}s_{13}e^{i\delta} & c_{12}c_{23} - s_{12}s_{23}s_{13}e^{i\delta} & s_{23}c_{13} \\ s_{12}s_{23} - c_{12}c_{23}s_{13}e^{i\delta} & -c_{12}s_{23} - s_{12}c_{23}s_{13}e^{i\delta} & c_{23}c_{13} \end{pmatrix}, \tag{1.2}
$$

where $s_{ij} = \sin\theta_{ji}$, $c_{ij} = \cos\theta_{ji}$, and δ is the CP-violating phase.

A more convenient parameterization introduced by Lincoln Wolfenstein [4] as an expansion in powers of λ is,

$$\begin{pmatrix} 1 - \frac{1}{2}\lambda^2 & \lambda & A\lambda^3(\rho - i\eta + \frac{i}{2}\eta\lambda^2) \\ -\lambda & 1 - \frac{1}{2}\lambda^2 - i\eta A^2\lambda^4 & A\lambda^2(1 + i\eta\lambda^2) \\ A\lambda^3(1 - \rho - i\eta) & -A\lambda^2 & 1 \end{pmatrix} + \mathcal{O}(\lambda^4),$$

(1.3)

where $\lambda = s_{12} = \sin\theta_c$, $A\lambda^2 = s_{23}$, and $A\lambda^3(\rho - i\eta) = s_{13}e^{-i\delta}$. This parameterization implies the hierarchy

$$|V_{ub}|^2 << |V_{cb}|^2 << |V_{us}|^2 << 1,$$ (1.4)

such that b quark has an inclination to decay into c rather than u.

The magnitude of entries can be determined from adequate weak decays. After measurements of the 4 real quantities in the Wolfenstein parametrization,

$$\begin{array}{ll} \lambda = 0.2253 \pm 0.0007, & A = 0.808^{+0.022}_{-0.015}, \\ \bar{\rho} = 0.132^{+0.022}_{-0.014}, & \bar{\eta} = 0.341 \pm 0.013, \end{array}$$

(1.5)

the CKM elements are [6]

$$\begin{pmatrix} 0.97428 \pm 0.00015 & 0.2253 \pm 0.0007 & 0.00347^{+0.00016}_{-0.00012} \\ 0.2252 \pm 0.0007 & 0.97345^{+0.00015}_{-0.00016} & 0.0410^{+0.0011}_{-0.0007} \\ 0.00862^{+0.00026}_{-0.00020} & 0.0403^{+0.0011}_{-0.0007} & 0.999152^{+0.000030}_{-0.000045} \end{pmatrix}.$$

(1.6)

Notice that the measured value is consistent with the unitary relations,

$$\begin{array}{l} |V_{ud}|^2 + |V_{us}|^2 + |V_{ub}|^2 = 1 \\ |V_{cd}|^2 + |V_{cs}|^2 + |V_{cb}|^2 = 1 \\ |V_{td}|^2 + |V_{ts}|^2 + |V_{tb}|^2 = 1 \end{array}$$

(1.7)

1.2 B Meson Physics

In 1977, the third generation bottom quark (b) was observed by the CFS[1] E288 experiment headed by Leon Lederman at Fermilab [5]. B mesons are the particles composed of a bottom antiquark ($\bar{b}$) and either a u quark or a d quark, leading to be charged (B^+) or neutral (B^0) respectively. Besides, a bottom antiquark and a strange quark (s) or a charm quark (c) form a strange B meson (B_s^0) or a charmed B meson (B_c^+). The properties of these B mesons are shown in Table 1.1.

---

[1]Columbia-Fermilab-Stony Brook collaboration

Table 1.1: Properties of B mesons.

Type	Quark content	I(J^P)	Rest mass (MeV/c^2)	Mean lifetime(ps)
B^+	$u\bar{b}$	$\frac{1}{2}(0^-)$	5279.17 ± 0.29	1.641 ± 0.008
B^0	$d\bar{b}$	$\frac{1}{2}(0^-)$	5279.50 ± 0.30	1.519 ± 0.007
B_s^0	$s\bar{b}$	$0(0^-)$	5366.3 ± 0.6	1.425 ± 0.041
B_c^+	$c\bar{b}$	$0(0^-)$	6277 ± 6	0.453 ± 0.041

To study the physics of B mesons, namely B physics, 2 B factories, KEKB(Belle) and PEP-II(BaBar), were built in the 1990s. Since the mass of $\Upsilon(4S)$ is only 20 MeV above $B\bar{B}$ threshold, and the branching fraction of $\Upsilon(4S)$ to $B\bar{B}$ is larger than 96% [6], both of the B factories chose to utilize e^+e^- collider with asymmetry energy in order to produce B mesons via the process $e^+e^- \to \Upsilon(4S) \to B\bar{B}$(Fig 1.5).
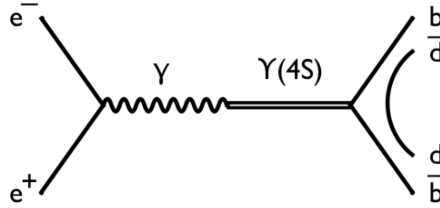
Figure 1.5: $e^+e^- \to \Upsilon(4S) \to B\bar{B}$ process.

1.3   Motivation

B meson can decay into final states with charmed or charmless hadrons through quark fragmentation and hadronization. The branching ratio of $B^+ \to p\bar{\Lambda}_{1520}$ decay, one of the simplest 2-body decay mode, has been measured by LHCb to the order $10^{-7} - 10^{-6}$, at the boundary to be observed with the current data sets accumulated at B-factories. Since $\bar{\Lambda}_{1520}$ decays to $\bar{p}$ and K^+ and the lifetime of $\bar{\Lambda}_{1520}$ is short enough to neglect, we believe it is a clear mode to study.
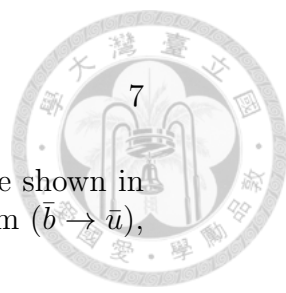
The leading Feynman Diagrams for $B^+ \to p\bar{\Lambda}_{1520} \to p\bar{p}K^+$ are shown in Fig 1.6. The penguin diagram ($\bar{b} \to \bar{s}$) dominates the tree diagram ($\bar{b} \to \bar{u}$), due to the latter be CKM suppressed.
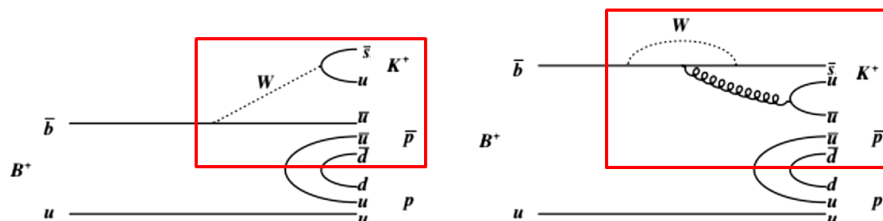
Figure 1.6: Feynman diagram of $B^+ \to p\bar{\Lambda}_{1520} \to p\bar{p}K^+$ process. The tree diagram is on the left, and the dominated penguin diagram is on the right.

Chapter 2

Belle Experiment

The Belle experiment is designed to investigating the CP violation effects. It is conducted by the Belle Collaboration, an international collaboration of more than 400 physicists and engineers from 16 countries, and located at the High Energy Accelerator Research Organization (KEK) in Tsukuba, Ibaraki Prefecture, Japan.(Fig 2.1) The Belle experiment includes 2 major facilities: KEKB accelerator and the Belle detector.
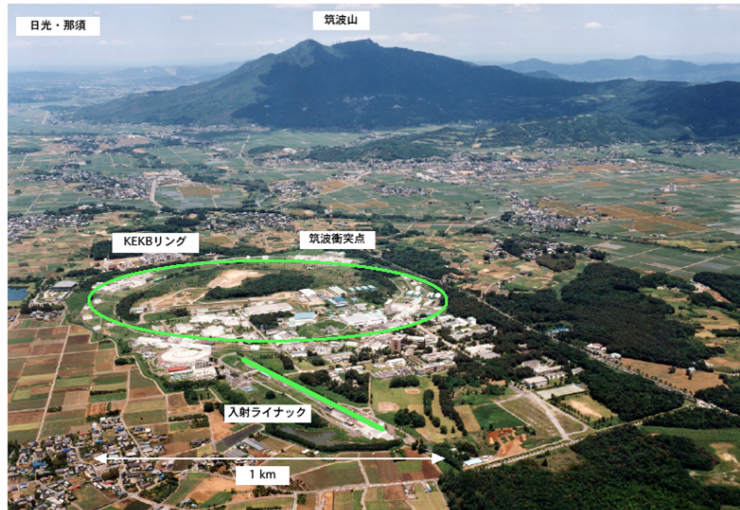
Figure 2.1: Bird's eye view of KEKB.

9
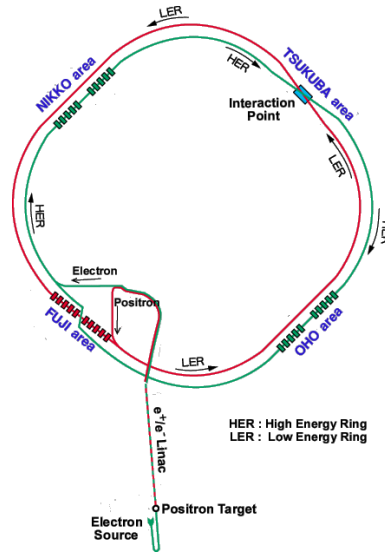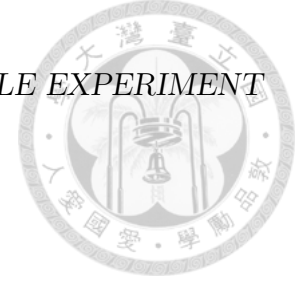
Figure 2.2: Configuration of the KEKB accelerator: The Belle detector is located in the interaction point in Tsukuba hall.

2.1   KEKB accelerator

KEKB [7], which stands for the KEK B-factory, is an asymmetric energy $e^- - e^+$ collider at KEK. The KEKB accelerator has 2 separate rings: a low-energy ring (LER) for positrons with 3.5 GeV beam energy while a high-energy ring (HER) for electrons with 8 GeV beam energy. Both rings are constructed side by side in the tunnel with a circumference of 3 km. To insure exactly the same circumference for the two rings, a cross-over design in Fuji area is built. (Fig 2.2) To reduce parasitic collisions near IP for reaching higher peak luminosities, the crossing angle of $e^- - e^+$ collision is set at ± 11 mrad.

For convenience, we define $\hat{z}$ to be the inverse direction of LER, and $\hat{x}$ be perpendicular to z-axis which let x-z plane containing both HER and LER. The KEKB is designed to operate with a peak luminosity at the order of 10^{34} cm^{-2}s^{-1}, corresponding to 10^8 $B\bar{B}$ pairs per year. Total integrated luminosity of 1052 fb^{-1} (including 772×10^6 $B\bar{B}$ pairs running at $\Upsilon(4S)$) was accumulated by Belle detector during the operation of KEKB, from Dec, 1998 to Jun, 2010. More parameters for the KEKB accelerator are listed in Table 2.1.

Table 2.1: Parameters of the KEKB accelerator

Ring		LER	HER	Unit
Energy	E	3.5	8.0	GeV
Circumference	C	3016.26		m
Luminosity	L	1×10^{34}		cm^{-2}s^{-1}
Crossing angle	θ_x	± 11		mrad
Tune shifts	ξ_x/ξ_y	0.039/0.052		
Beta function at IP	β_x^*/β_y^*	0.33/0.01		m
Beam current	I	2.6	1.1	A
Natural bunch length	σ_z	0.4		cm
Energy spread	σ_ε	7.1×10^{-4}	6.7×10^{-4}	
Bunch spacing	s_b	0.59		m
Particles/bunch	N	3.3×10^{10}	1.4×10^{10}	
Emittance	$\varepsilon_x/\varepsilon_y$	$1.8 \times 10^{-8}/3.6 \times 10^{-10}$		
Synchrotron	ν_s	$0.01 \sim 0.02$		
Betatron tune	ν_x/ν_y	45.52/45.08	47.52/43.08	
Energy loss/turn	U_0	$0.81^\dagger/1.5^{\dagger\dagger}$	3.5	MeV
RF voltage	V_c	$5 \sim 10$	$10 \sim 20$	MV
RF frequency	f_{RF}	508.887		MHz
Harmonic number	h	5120		
Longitudinal damping time	τ_ε	$43^\dagger/23^{\dagger\dagger}$	23	ms
Total beam power	P_b	$2.7^\dagger/4.5^{\dagger\dagger}$	4.0	MW
Radiation power	P_{SR}	$2.1^\dagger/4.0^{\dagger\dagger}$	3.8	MW
HOM power	P_{HOM}	0.57	0.15	MW
Bending radius	ρ	16.3	104.5	m
Length of bending magnet	l_B	0.915	5.86	m

$\dagger$: without wigglers, $\dagger\dagger$: with wigglers
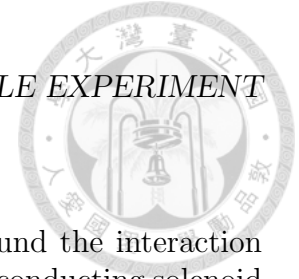
2.2   Belle Detector

As shown in Fig 2.3, the Belle detector is mounted around the interaction point (IP). The beampipe and its surrounding 1.5T superconducting solenoid go through the sub-detectors:

B-meson decay vertices are measured by SVD situated just outside of a cylindrical beryllium beam pipe; charged particle tracking is provided by dE/dx measurement in CDC; particles are identified with the information measured by CDC, ACC, and TOF;(See section 3.3.3) electromagnetic showers are detected in ECL, whereas Muon and K_L detected in KLM. The above sub-detectors cover the θ region extending from $17°$ to $150°$, and a part of the uncovered small-angle region is instrumented with a pair of BGO crystal arrays (EFC). The performance of the detectors are summarized in Table 2.2 and the descriptions of each sub-detector are included in the following sections. (Since electrons and muons are not involved in our study, the detail of KLM is skipped.)

2.2.1   Beam Pipe

The precise determination of decay vertices is an essential feature of the Belle experiment. Coulomb scattering in the beam pipe wall (and also the 1st layer of the silicon detector) affects the z-vertex position resolution. Therefore, minimizing the thickness of the beam pipe is necessary. The originally designed beam pipe has an inner / outer radius of 2.0 / 2.3 cm. The central part (-4.6 cm $\leq z \leq 10.1$ cm) of the beam pipe consists of double beryllium cylinders of 0.5 mm thickness. Moreover, the aperture of the beam pipe near IP is designed to avoid hitting by the synchrotron radiation from the final-focus quadrupole magnets (QCS) and other magnets going through. Besides, a 2.5 mm gap between the inner and outer walls of the cylinder provides a helium gas channel for cooling.

Belle Detector
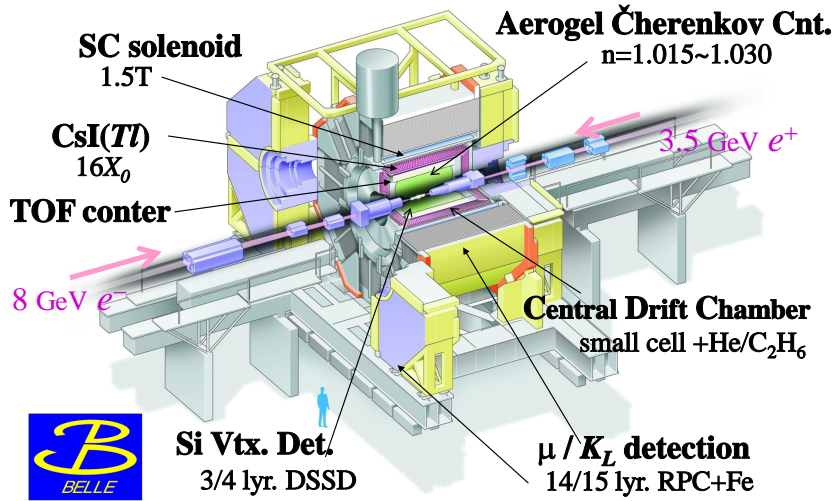
(a) Cut view of the Belle detector.
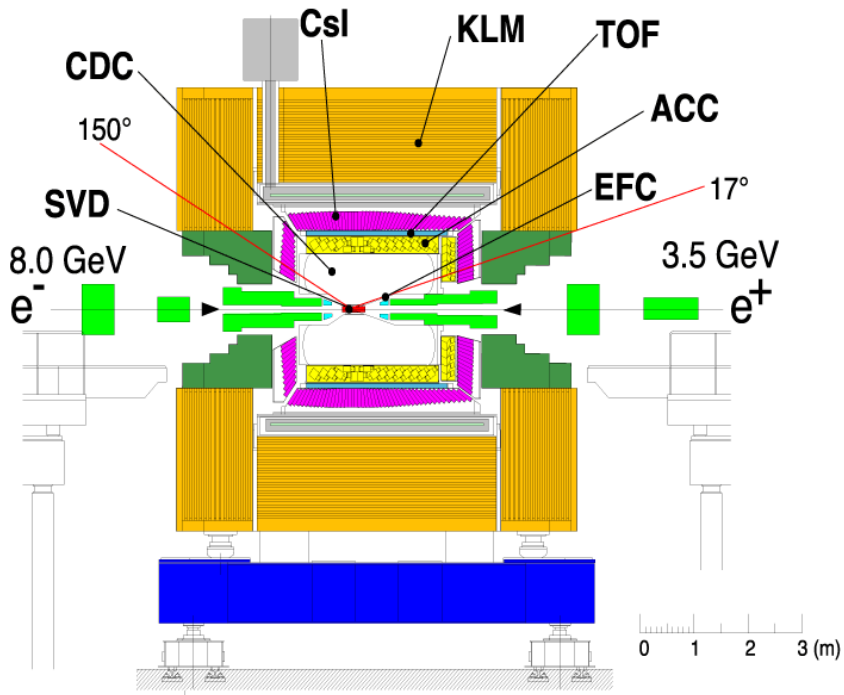
(b) Side view of the Belle detector.

Figure 2.3: Configuration of the Belle detector.

Table 2.2: Performance parameters for the Belle detector. There were two configurations of inner detectors used to collect two data sets, DS-I and DS-II, corresponding to a 3-layer SVD1 and a 4-layer SVD2 with a smaller beam pipe, respectively.

Detector	Type	Configuration	Readout	Performance
Beam pipe for DS-I	Beryllium double wall	Cylindrical, r = 20mm, 0.5/2.5/0.5(mm) = Be/He/Be w/ He gas cooled		
Beam pipe for DS-II	Beryllium double wall	Cylindrical, r = 15mm, 0.5/2.5/0.5(mm) = Be/PF200/Be		
EFC	BGO	Photodiode readout Segmentation : 32 in ϕ; 5 in θ	160×2	Rms energy resolution: 7.3% at 8 GeV 5.8% at 2.5 GeV
SVD1	Double-sided Si strip	3-layers: 8/10/14 ladders Strip pitch: 25(p)/50(n)μm	ϕ: 40.96k z: 40.96k	$\sigma(z_{CP}) \sim 78.0\mu$m for $B \to \phi K^0 2_s$
SVD2	Double-sided Si strip	4-layers: 6/12/18/18 ladders Strip pitch: 75(p)/50(n)μm (layer1-3) 73(p)/65(n)μm (layer4)	ϕ: 55.29k z: 55.296k	$\sigma(z_{CP}) \sim 78.9\mu$m for $B \to \phi K_s^0$
CDC	Small cell drift chamber	Anode: 50 layers Cathode: 3 layers r = 8.3 - 86.3 cm $-77 \leq z \leq 160$ cm	Anode: 8.4k Cathod: 1.8k	$\sigma_{r\phi} = 130\mu$m $\sigma_z = 200 \sim 1400\mu$m $\sigma_{Pt}/Pt = 0.3\%\sqrt{p_t^2 + 1}$ $\sigma_{dE/dx} = 0.6\%$
ACC	Silica aerogel	960 barrel/228 end-cap FM-PMT readout		$N_{p.e.} \geq 6$ K/π seperation: $1.2 < p < 3.5$GeV/c
TOF	Scintillator	128 ϕ segmentation r = 120 cm, 3-cm long	128×2	$\sigma_t = 100$ ps K/π seperation:
TSC		64 ϕ segmentation	64	up to 1.2 GeV/c
ECL	CsI (Towered-structure)	Barrel: r = 125 - 162 cm End-cap: z = -102 cm and +196cm	6624 1152(F) 960(B)	$\sigma_E/E = 1.3\%/\sqrt{E}$ $\sigma_{pos} = 0.5$ cm/$\sqrt{E}$ (E in GeV)
KLM	Resistive plate counters	14 layers (5 cm Fe + 4cm gap) 2 RPCs in each gap	θ: 16k ϕ: 16k	$\Delta\phi = \Delta\theta = 30$mr for K_L $\sim 1\%$ hadron fake
Magnet	Supercon.	Inner radius = 170 cm		B=1.5T

2.2.2 Silicon Vertex Detector (SVD)

The $\sim 100\ \mu$ m position resolution of SVD is primarily for the measurement of the difference in z-vertex positions for $B\bar{B}$ pairs. The SVD consists of 3 layers, 32 ladders of double-sided silicon strip detectors (DSSD) and covers most part of solid angle ($23° < \theta < 139°$). Each DSSD has 1280 sense strips and 640 readout pads on opposite sides. The designed configuration is shown in Fig 2.4. The z-strip / ϕ strip pitch is 42 / 25 μ m, and the active regions are 53.5×32.0 / $54.5 \times 32.0 mm^2$ on the z-side / ϕ -side.

To ensure that the SVD tracks match the tracks detected by CDC, higher SVD strip yields and better S/N ratios are needed. Therefore, in 2003, the SVD system was upgraded to the so-called SVD2, consisting of 4 layers of DSSDs with a larger coverage ($17° < \theta < 150°$, same as CDC). 2 types of DSSD are used for different layers. Basically, the SVD2 improves the detecting efficiency a bit and operates in a similar way to SVD1. The comparison is shown in Fig 2.5.
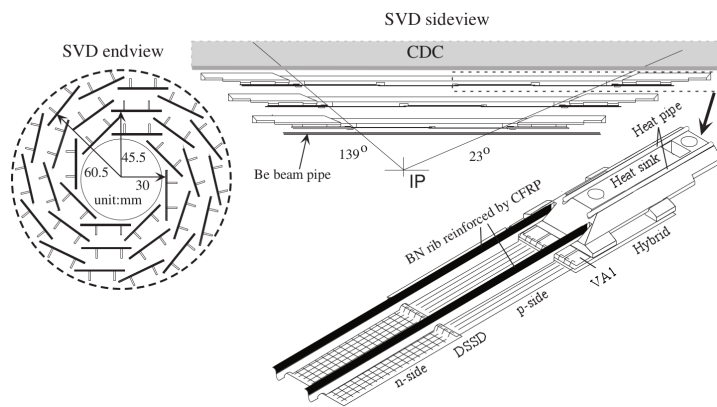
Figure 2.4: Configuration of SVD

2.2.3 Extreme Forward Calorimeter (EFC)

EFC is designed for improving the experimental sensitivity to some physics processes such as $B \rightarrow \tau\nu$ and two-photon physics. It also reduces backgrounds for CDC. Moreover, it is used as a beam monitor for the KEKB control and a luminosity monitor for the Belle experiment. The EFC detector, surrounding the beam pipe, is attached to the front faces of the cryostats of the compensation solenoid magnets of the KEKB accelerator. It covers the angular range from $6.4°$ to $11.5°$ in the forward (e^-) direction and $163.3°$
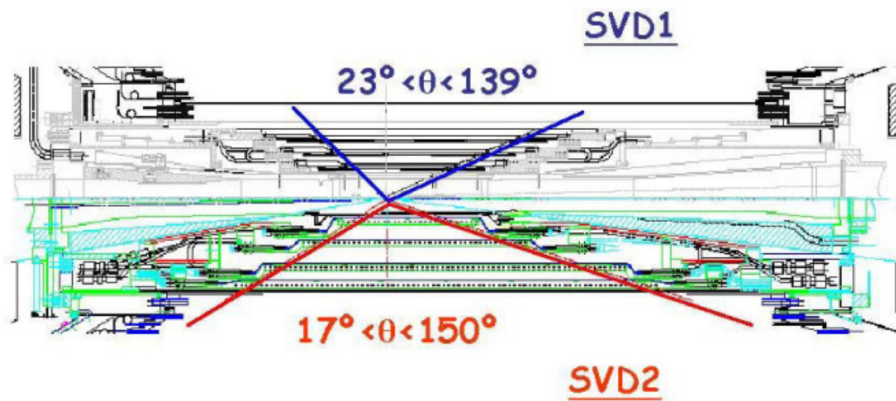
(a) Side view comparison of SVD1 and SVD2.

(b) End view comparison of SVD1 and SVD2.

Figure 2.5: Graphical illustration of sub-detector SVD1 and SVD2.

to 171.2° in the backward (e^+) direction. To endure such long-term and high level radiation, radiation-hard BGO (Bismuth Germanate, $Bi_4Ge_3O_{12}$) crystal is chosen to construct EFC. There are 320 channels with photodiode readout in EFC, provi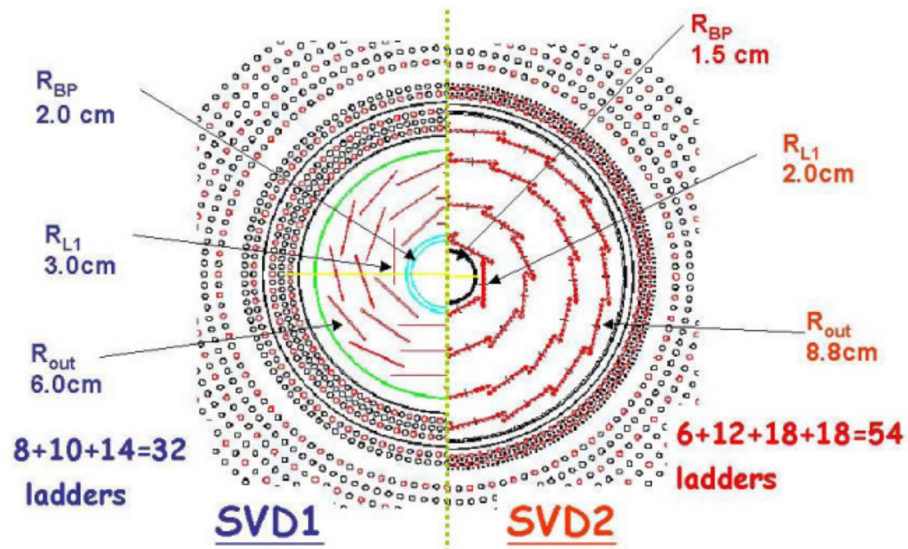ding an energy resolution of 7.3%/5.8% for the forward / backward EFC. An isometric view of the EFC detector is shown in Fig 2.6.
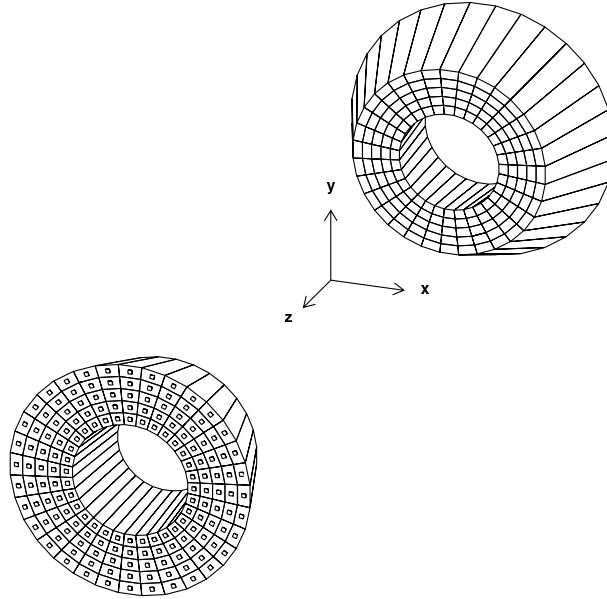
Figure 2.6: Isometric view of the BGO crystals of the forward and backward EFC detectors.

2.2.4 Central Drift Chamber (CDC)

CDC is exploited to measure the transverse momentum (P_t) of charged particles by the curvatures in the transverse plane. It also measure their momentum in the z-direction (P_z) from the helical track information and P_t. Beside P_t and P_z, CDC measures the energy loss (dE/dx) of charged particles as well.

The spatial resolution ranges from 120 to 150 μm, so precise that the resolution of P_t is smaller than 1% most of the time. Since gas with low atomic number minimize Coulomb scattering that effects the momentum resolution and ethane provides good dE/dx resolution, 50% He and 50% ethane is used in CDC. Such high resolution makes particle identification more precise. (Fig 2.8)

The coverage of CDC is $17° < \theta < 150°$, consisting of 50 layers and 3 cathode strip layers. It has a total of 8400 drift cells. The inner / outer radius of CDC is 103.5 / 874 mm, as shown in Fig 2.7.
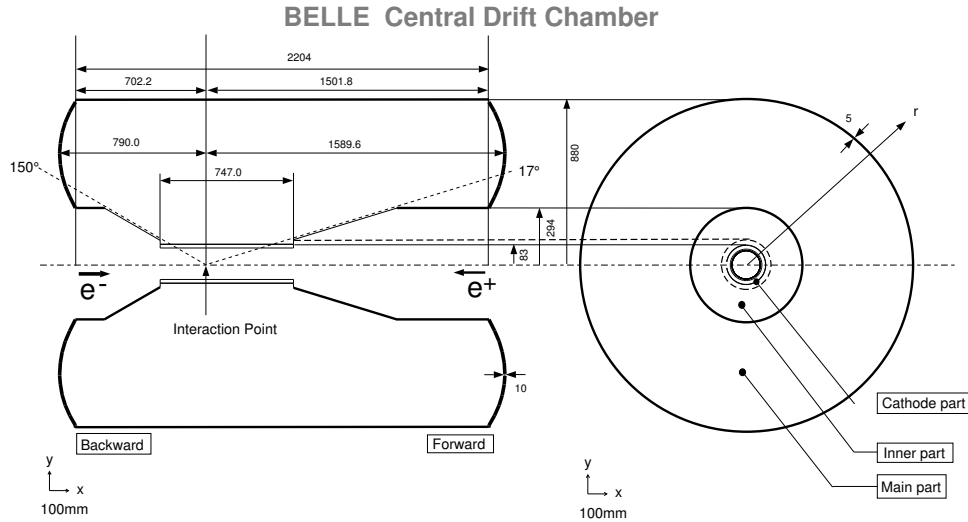
Figure 2.7: Overview of the CDC structure. The lengths in the figure are in units of mm.

2.2.5   Aerogel Cherenkov Counter System (ACC)

Although dE/dx measurement (by CDC) and time-of-flight measurement (by TOF) provide useful separation of K/π , an array of silica aerogel threshold Cherenkov counters is built to distinguish π from K in further extensive momentum coverage. (ACC covers 17° - 127° in polar angle.)

Fig 2.9 shows the arrangement of ACC, containing 960 / 228 counter modules in barrel / end-cap part, and Fig 2.10 shows the schematic drawing of the 2 types. These modules are segmented into 60 cells in the ϕ direction for the barrel ACC, and arranged in 5 concentric layers for the end-cap part. The refractive indices of aerogels ranges from 1.01 to 1.03 depending on their spatial position, and the fine-mesh photomultiplier tubes (FM-PMTs) with corresponding diameters to obtain uniform response of Cherenkov light.

Figure 2.8: Scatter plot for dE/dx versus momentum. Expected results for π, K, p and e are shown by solid curves. The unit of the momentum is GeV/c.
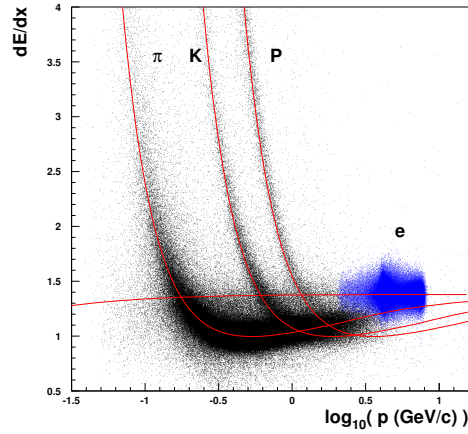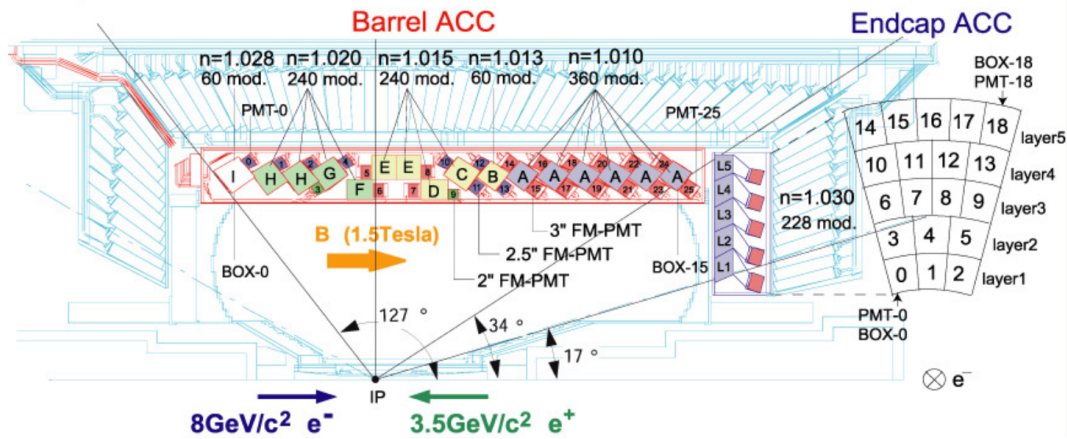

Figure 2.9: Arrangement of ACC at the central part of the Belle detector. The index of refraction (n) is for each ACC module.
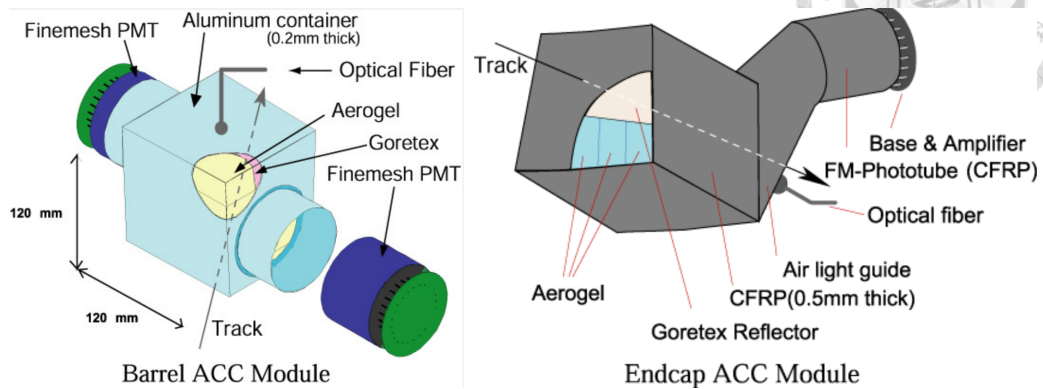
Figure 2.10: Schematic drawing of a typical ACC counter module: (a) barrel and (b) end-cap ACC.

2.2.6   Time-of-Flight Counters (TOF)

TOF is used to identify charged particles with momenta below 1.2 GeV/c (almost 90% of the particles produced in $\Upsilon(4S)$ decays) and as a trigger due to fine time resolution (100 ps). The mass (M_{track}) distribution is shown in Fig 2.12.

The whole TOF system consists of 128 TOF counters and 64 trigger scintillation counters (TSC) with 70 kHz trigger rate preventing trigger queue from pile-up. A TOF / TSC module is constructed by 2 TOF and 1 TSC, as shown in Fig 2.11.

The length of the flight path is 1.2 m, and coverage of polar angle is $17° < \theta < 127°$, same as that of CDC.

2.2.7   Electromagnetic Calorimeter (ECL)

ECL is designed to detect the energy and position of photons, and to identify electrons as well, by computing the ratio E/p (momentum p is provided by CDC).

The configuration is shown in Fig 2.13, and Table 2.3 lists some parameters. All crystals are shaped in a half-tower and point almost to the IP with a small tilt angle ($1.3° - 4°$) to avoid small leakage of photons from the gaps between the crystals. Moreover, the gaps between the end-cap and barrel parts are so small that only 3% of total acceptance is missing.

ECL use CsL(Tl) crystals as its scintillator. Since smaller size has better position resolution, while larger size having better energy resolution due
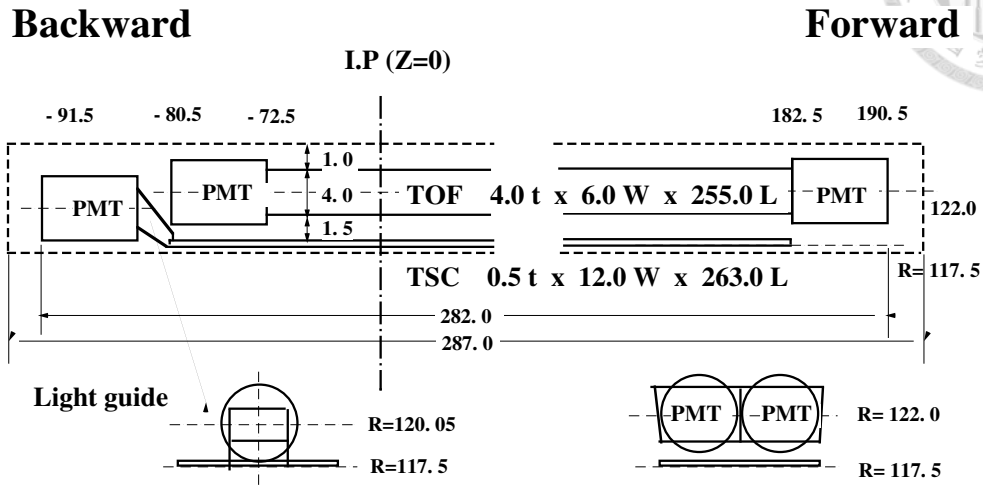
Figure 2.11: Illustration of a TOF/TSC module. The unit of length is in mm.
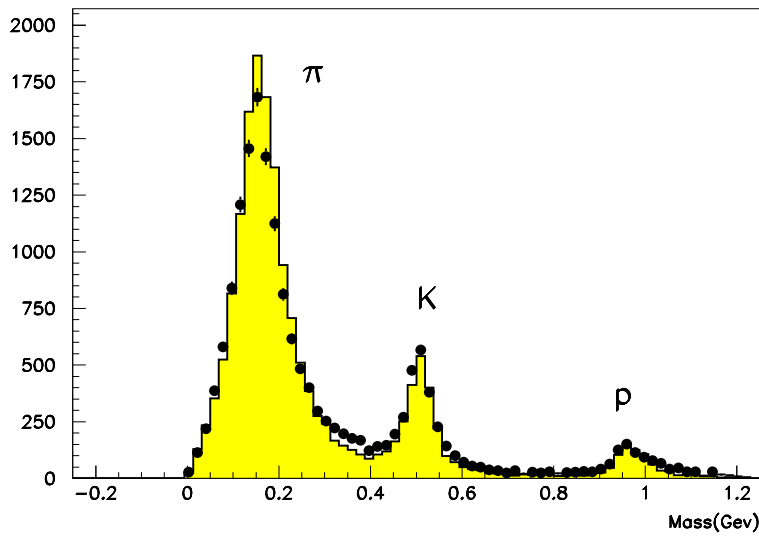
Figure 2.12: Mass distribution from TOF measurements for particle momenta below 1.2 GeV/c.

to smaller crystal interfaces and lower cost, the cross-sectional area varies significantly from $44.5^2/54^2 mm^2$ to $70.8^2/82^2 mm^2$ for the front / rear faces. By contrast, the length of crystals are all 30 cm $(16.2X_0)$ to avoid deterioration of energy resolution. After some calibrations, the energy resolution reached to 1.7% for the barrel ECL, and 1.74% and 2.85% for the forward and backward ECL respectively.
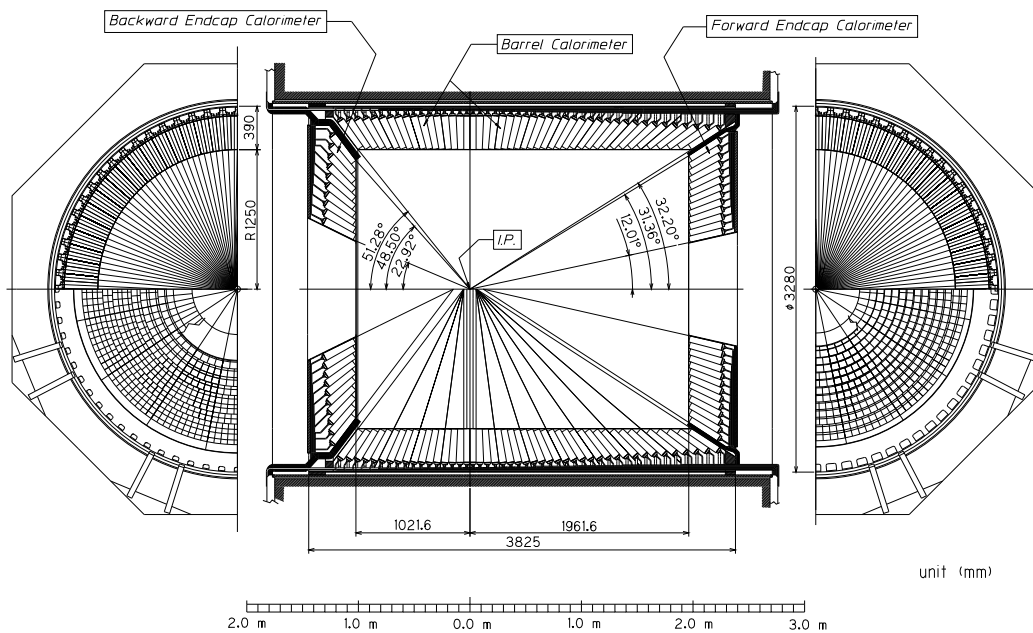
Figure 2.13: Overall configuration of ECL.

2.3   Trigger and Data Acquisition

At a luminosity of 10^{34} cm^{-2}s^{-1}, the trigger rate due to beam background is expected to be $\sim$ 100 Hz based on simulation studies. The trigger system is required to be robust against unexpectedly high beam background rates, and should be flexible so that background rates are kept within the tolerance of the data acquisition system (DAQ) 500 Hz, while the efficiency for events of interest is kept high. The redundant triggers to keep the efficiency high even for varying conditions is also considered.

Table 2.3: Geometrical parameters of ECL.

Item	θ coverage	θ seg.	ϕ seg.	No. of crystals
Forward end-cap	$12.4° - 31.4°$	13	$48-144$	1152
Barrel	$32.2° - 128.7°$	46	144	6624
Backward end-cap	$130.7° - 155.1°$	10	$64-144$	960

The Belle trigger system consists of the level-1 hardware trigger and the level-3 software trigger. The latter has been designed to be implemented in the online computer farm. Figure 2.14 shows the schematic view of the level-1 trigger system [8]. There are sub-detector trigger systems and a central trigger system called the Global Decision Logic (GDL). The sub-detector trigger systems are based on two categories: CDC and TOF are used to yield trigger signals for charged particles, while ECL trigger system provides triggers based on energy deposit and cluster counting of crystal hits. The KLM trigger gives additional information on muons and the EFC triggers are used for tagging two photon events and Bhabha events.

All the sub-trigger signals arrive at GDL within 1.85 μs after the event occurrence, and the level-1 final trigger signal is issued 2.2 μs after event crossing. The timing of the trigger is primarily determined by the TOF trigger which has the time jitter less than 10 ns. ECL trigger signals are also used as timing signals for events in which the TOF trigger is not available.

The DAQ system is designed to be tolerable to a trigger rate of up to 500 Hz. A distributed-parallel system has been devised such that it works at 500 Hz with a deadtime fraction of less than 10%. The global scheme of the system is illustrated in Figure 2.15. The DAQ system is segmented into 7 subsystems running in parallel, each handling the data from a sub-detector. Data from each subsystem are combined into a single event record by an event builder. Its output is transferred to an online computer farm, where another level of event filtering is done after fast event reconstruction. The data are then sent to a mass storage system located at the computer center via optical fibers.
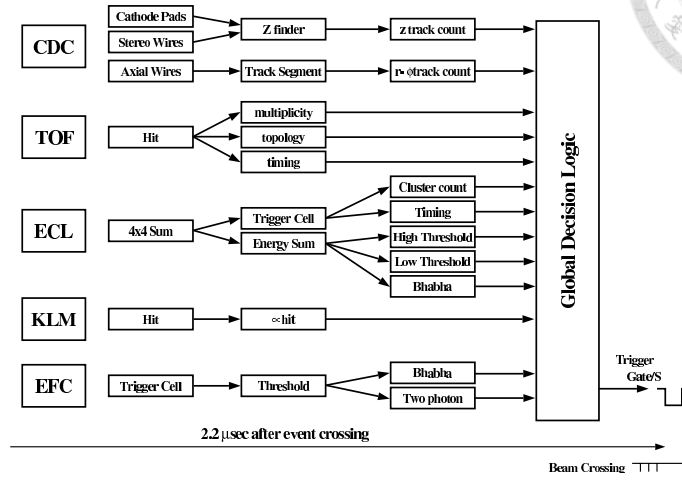
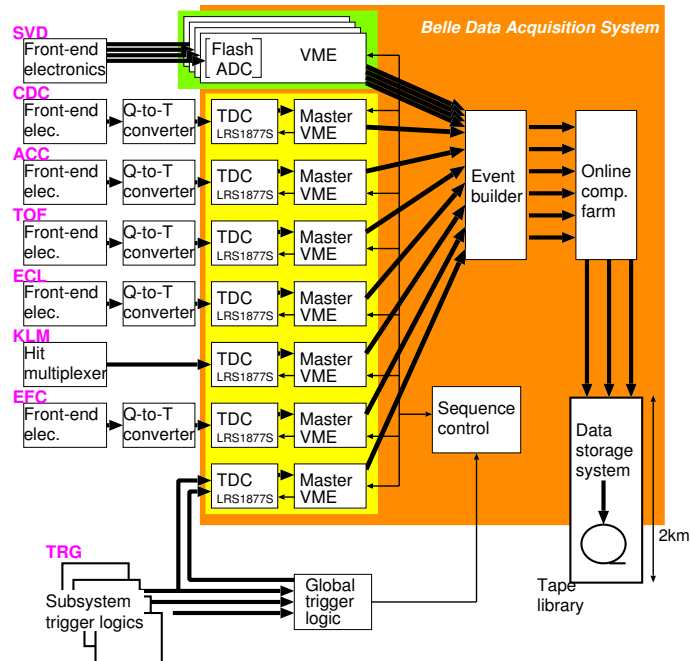Figure 2.14: The Level-1 trigger system for the Belle detector.

Figure 2.15: Belle DAQ system overview.

Chapter 3

Analysis

3.1 Blind Analysis

This analysis employed the blind analysis which is completely based on the Monte Carlo simulation for signal selection. The blind analysis method is a good experimental way to reduce or eliminate experimental bias, for it being performed without looking at the answer, or the real data. Operating on the Monte Carlo instead of the real data prevents experimentalists from adjusting the parameters towards prior results or theoretical expectations. Therefore, the blind analysis method, which is commonly used in particle physics, is employed in the study. The commonly used tools and methods involved in this analysis are shown in section 3.2 and 3.3 respectively.

3.2 Analysis Tools

3.2.1 BASF

Belle Analysis Framework (BASF) is the software framework to process data for Belle. BASF consists of 2 subsystems: the BASF kernel and the UI. The "clients" connect to the "server", the BASF kernel, via the UI. (Fig3.1)

The framework has the following features: module and path structure, dynamic linking of modules, multi-language support, unified data access method by Panther, parallel event-by-event processing, etc. An analysis code is written as a module, dynamically linked to BASF. The order of execution of modules is defined by creating a path. After then, Panther, a home-made memory manager, is utilized for data management.
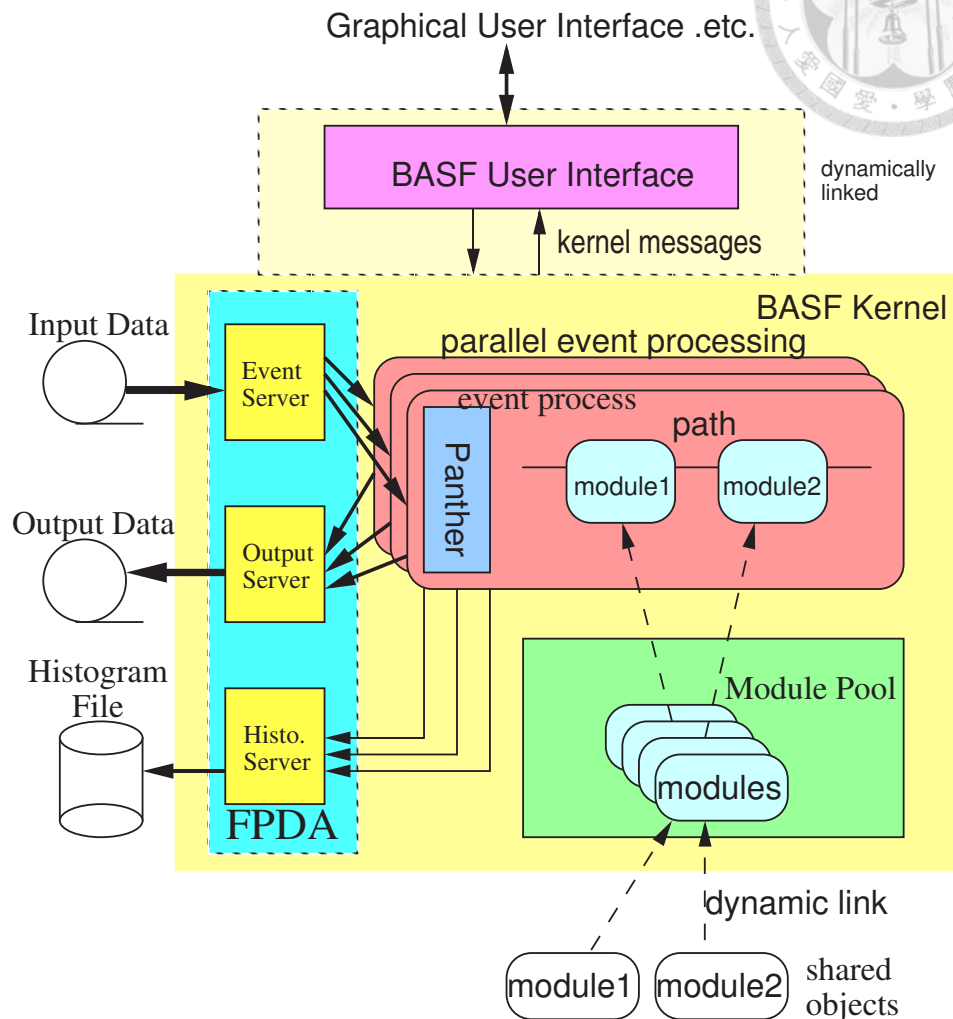
Figure 3.1: Schematic view of the BASF framework

3.2.2   EvtGen and GSIM

The EvtGen package [12] is initialized by CLEO and developed by BaBar. Written in C++ language, EvtGen implements many well-described decay models, including continuum $q\bar{q}$ events, for B physics studying. In this framework, defining a new particle or a new decay model for event generation is allowed.

GSIM, an abbreviation for GEANT-based Detector Simulation, is used to simulate the behavior of detectors interacting with elementary particles

passing through. GSIM was originally designed for HEP experiments, but now applies to other research areas as well.

EvtGen and GSIM are 2 important packages for the Monte Carlo simulation at Belle.

3.2.3   ROOT and RooFit

Although PAW (Physics Analysis Workstation) is still a popular software tool for data analysis in High Energy Physics, it could not be scaled up to the challenges offered by the Large Hadron Collider and SuperKEKB. Therefore, packages for data analysis, such as ROOT, were developed [16].

ROOT is an Object Oriented framework written mainly in C++, containing an efficient hierarchical OO database, a C++ interpreter, advanced statistical analysis (multi-dimensional histogram, fitting, minimization, cluster finding algorithms) and visualization tools.

RooFit, a part of ROOT packages, is a complete toolkit for curve fitting and data distribution modeling.

## 3.3   B meson reconstruction

3.3.1   Data Sample

The integrated luminosity collected by the Belle detector at KEKB e^+e^- collider is about 710 fb^{-1} at the $\Upsilon(4S)$ resonance. The corresponding number of $B\bar{B}$ events is 771.581 ± 10.566 million, and that is the number defined as 1 stream in the Monte Carlo simulation.

3.3.2   Tracking

The tracks of charged particles are reconstructed with the information from SVD, CDC and TOF. TOF provides the event timing, and CDC reconstructs the tracks, also extrapolated by SVD detector. These detectors make the momenta and the trajectories of the charged particles accurate, leading to the precision of vertex reconstruction.

In order to rule out the secondary tracks generated by hadronic interaction, $|dr| < 0.3$ cm and $|dz| < 3$ cm are required, where dr and dz defined as the distance from IP (interaction point) in the transverse $(x - y)$ plane and the $z-$direction respectively.
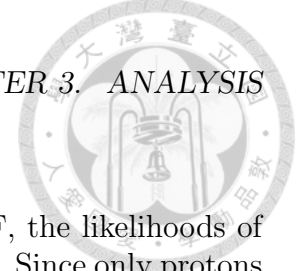
3.3.3   Particle Identification

According to the information from SVD, CDC and TOF, the likelihoods of charged particles, $\mathcal{L}_p$, $\mathcal{L}_K$, $\mathcal{L}_\pi$, $\mathcal{L}_e$ and $\mathcal{L}_\mu$, are determined. Since only protons and Kaons are considered in this analysis, particles with $\mathcal{L}_e > 0.95$ and those with $\mathcal{L}_\mu > 0.95$, i.e., lepton-like, are excluded.

To distinguish p and K from π, we define likelihood ratio $\mathcal{LR}_{X/Y}$ as $\mathcal{L}_X/(\mathcal{L}_X + \mathcal{L}_Y)$. A proton is identified with the conditions $\mathcal{LR}_{p/K} > 0.6$ and $\mathcal{LR}_{p/\pi} > 0.6$. Similarly, a Kaon is identified with the conditions $\mathcal{LR}_{K/\pi} > 0.6$ from the remaining charged particles.

3.3.4   Selection Summary

Besides the tracking constraints and particle identification, we also trimmed the events out of the range of energy difference (de) and the range of constrained mass of B meson (M_{bc}). The certain 2-dimension range of ΔE-M_{bc} is called the "Sample Box".

The principle of selection is to keep most signal events (up to 3 $\sigma \approx 99.7\%$ see Fig 3.2), therefore the preliminary selections are very loose. The summary of the preliminary selection range is shown in Table 3.1.

Table 3.1: Preliminary Selection

Track Impact Parameter	$\lvert dr \rvert < 0.3$ cm
	$\lvert dz \rvert < 3$ cm
Particle Identification	$\mathcal{L}_e < 0.95$
	$\mathcal{L}_\mu < 0.95$ (Both required)
$p^{\pm}$	$\mathcal{LR}_{p/K} > 0.6$
	$\mathcal{LR}_{p/\pi} > 0.6$
$K^{\pm}$	$\mathcal{LR}_{K/\pi} > 0.6$
	($\mathcal{LR}_{p/K} < 0.6$ or $\mathcal{LR}_{p/\pi} < 0.6$)
Sample Box	
M_{bc}	$5.20 < M_{bc} < 5.29$ GeV
de	$\lvert de \rvert < 0.24$ GeV
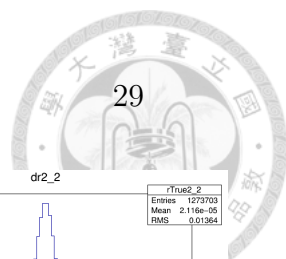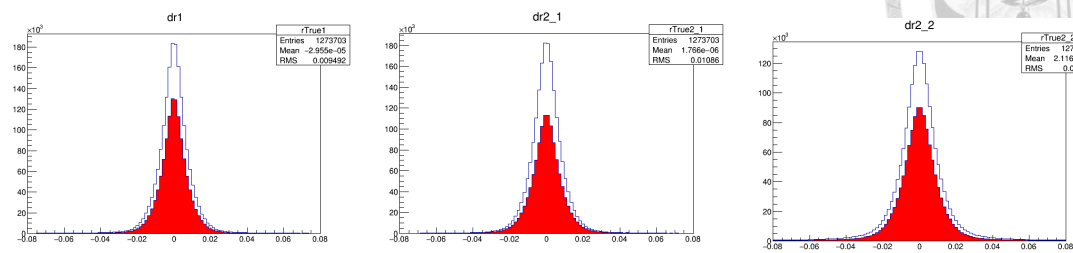
(a) dr for p(left), $\bar{p}$(middle) and K(right)
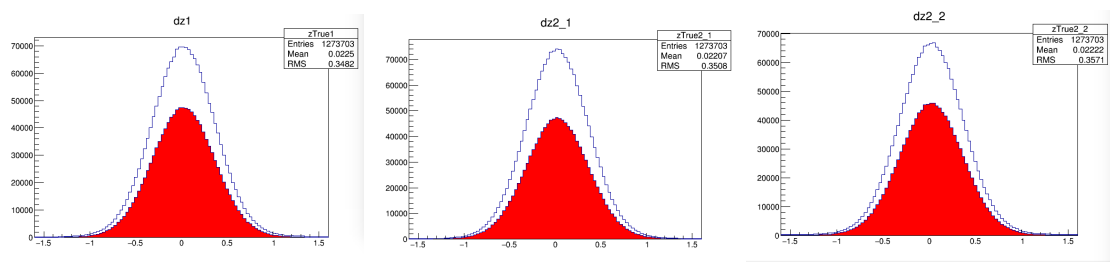
(b) dz for p(left), $\bar{p}$(middle) and K(right)
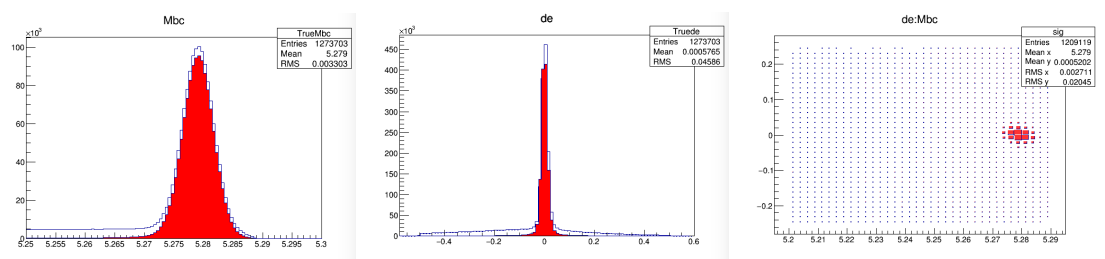
(c) Mbc(left), de(middle) and $de - Mbc$(right)

Figure 3.2: Distributions of dr and dz, M_{bc}, de for signal MC. The Monte Carlo true events are red-filled.

3.4   Background Suppression

Continuum background ($e^+e^- \to q\bar{q}$, where q denotes a quark: u, d, s or c) and generic B background ($b \to c$ transition including mixed and charged decay) are the main background of B meson analysis. In this section, the methods for background suppression will be introduced.

We study the backgrounds with Monte Carlo data based on the new tracking algorithm, with 5 stream of events for each.

3.4.1   NeuroBayes (NB)

NeuroBayes method is a multivariate analysis tool that can help us optimize the purity and efficiency of the signal. NB is not just a kind of neural network but also involving weight decay, Bayesian approaches and other algorithms. To begin with, some samples in both signal and background events are used to train the model. Only part of variables (better independent of each other) of events are chosen in the training. NB first transforms the input variables nonlinearly into flat distributions then into Gaussians, so the variables can be decorrelated and the insignificant ones are pruned. After that, NB finds another set of variables, where only one variable is correlated with the target variable. This new variable, called NB output (O_{NB}) in our study and ranging from 1 (signal-like) to -1 (background-like), has all the separating information from all other variables. After training, each event of the data can be told by the model whether it is more like a signal or a background, by given an number O_{NB}. We choose the O_{NB} cut to maximize the signal-to-noise ratio, by $\mathcal{F}.\mathcal{O}.\mathcal{M}.$, mentioned in Section 3.4.3.
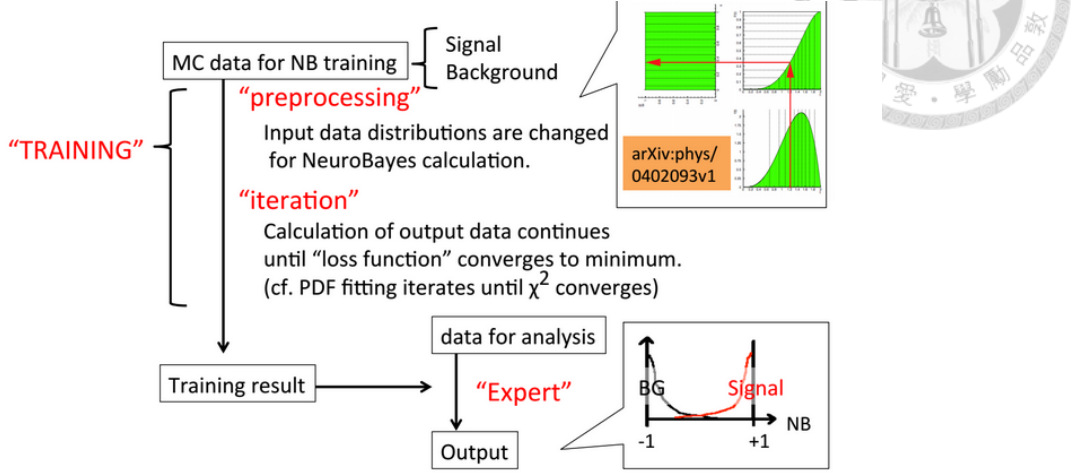
Figure 3.3: Work flow of NeuroBayes

3.4.2 Continuum Background

The continuum background dominates generic B background by 3 times, thus the suppression is important. Since $q\bar{q}$ events are more jet-like than the spherical $B\bar{B}$ ones (including the signal), shape variables are employed to NeuroBayes to help distinguishing continuum background from $B\bar{B}$ events.

We use the following shape variables:

- Kakuno SFW (KSFW)
  KSFW is one of the modified Super Fox-Wolfram (SFW), defined as:

$$KSFW \equiv \sum_{l=0}^{4} R_l^{so} + \sum_{l=0}^{4} R_l^{oo} + \gamma \sum_{l=0}^{N_t} |(P_t)_l| \qquad (3.1)$$

and the terms of KSFW is like

$$R_l^{so} = \frac{\alpha_c (H_c)_l^{so} + \alpha_n (H_n)_l^{so} + \alpha_m (H_m)_l^{so}}{E_{beam} - \Delta E} \qquad (3.2)$$

We can see that KSFW involves the term of total transverse momentum $(\sum P_t)$ and $(H_c)_l^{so}$, $(H_n)_l^{so}$, $(H_m)_l^{so}$. The last 3 terms are the ratio of nth-order to zeroth-order Super Fox-Wolfram (SFW) moments:

charged particles from B candidate and the remaining charged ones ($(H_c)_l^{so}$, 5 variables for $l = 0-4$); the neutral particles from B candidate and the remaining neutral ones ($(H_n)_l^{so}$, 3 variables for $l = 0, 2, 4$); the neutral particles from B candidate and the total missing momentum ($(H_m)_l^{so}$, 3 variables for $l = 0, 2, 4$); the charged and neutral particles excluding the particles from B candidate ($(H_m)_l^{oo}$ to calculate R_l^{oo}, 5 variables for $l = 0-4$).

Missing mass counts for NeuroBayes method because it is related to KSFW.

- Thrust Angle $(\cos\theta_T)$ and Sphericity
  The thrust angel θ_T is defined as the angle between the thrust axis $\vec{n}_T$ of the B candidate and that of the remaining particles. The thrust axis $\vec{n}_T$ is defined as the direction that maximize $T(\vec{n})$

$$
T(\vec{n}) = \frac{\sum\limits_{i=1}^{N}\left|\vec{P}_i \cdot \vec{n}\right|}{\sum\limits_{i=1}^{N}\left|\vec{P}_i\right|}, \tag{3.3}
$$

  where N is the number of daughter particles used to reconstruct B candidates and $\vec{P}_i$ is the 3-momentum of i-th daughter particle of B candidates.

  The distribution of $\cos\theta_T$ has peaks near ± 1 for $q\bar{q}$ due to jet-like event shape, whereas for $B\bar{B}$ is much flatter.

  Sphericity is the quantity to describe how "spher-like" it is. Sphericity can be obtained by calculating the ratio of magnitude of total transverse momentum to total momentum. In $q\bar{q}$ events, most are along the thrust axis, leading to small transverse momentum then low sphericity.

- B Flight Direction $(\cos\theta_B)$ and Vertex Difference ΔZ
  The θ_B is the angle between the flight direction of B and the beam direction in the $\Upsilon(4S)$ rest frame. The distribution of $\cos\theta_B$ obeys $1-\cos^2\theta_B$ (based on angular momentum conservation quantum physics) for $B\bar{B}$ events and is roughly flat for non-$B\bar{B}$ events.

  The vertex difference ΔZ is defined by that between the B candidate and the accompanying B. The distribution of ΔZ of $q\bar{q}$ events

is narrower because quarks cannot be isolated due to color confinement.

To sum up, the above variables are used for training in NeuroBayes method. Fig 3.4 shows the NB outputs. We will choose the cut in the next subsection.
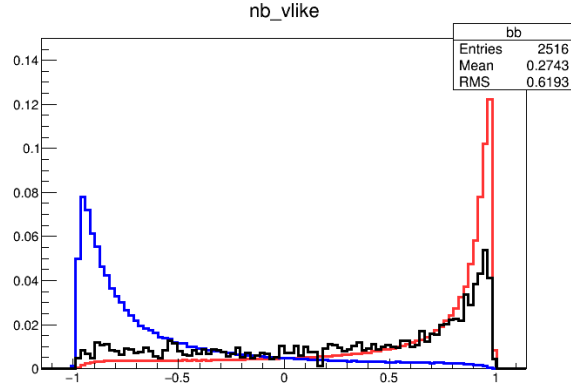

Figure 3.4: The NB output distribution O_{NB} of signal (red), $q\bar{q}$(blue) and $B\bar{B}$(black)

3.4.3   Figure of Merit ($\mathcal{F}.\mathcal{O}.\mathcal{M}.$)

To optimize the O_{NB} cut, i.e., to maximize the statistical significance of signal and to maximize signal-to-noise ratio, the quantity called Figure of Merit ($\mathcal{F}.\mathcal{O}.\mathcal{M}.$) is considered:

$$\mathcal{F}.\mathcal{O}.\mathcal{M}. = \frac{N_{sig}}{\sqrt{N_{sig} + N_{bg}}} \quad (3.4)$$
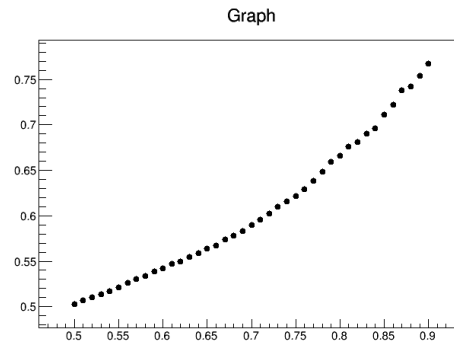
where the expected value N_{sig} is calculated by

$$N_{sig} = N_{B\bar{B}} \times \mathcal{B} \times \epsilon_{MC,sig}, \quad (3.5)$$

and

$$\epsilon_{MC,sig} = \frac{N_{remainaftercut}}{N_{generated}} \quad (3.6)$$

is the efficiency of MC.

Figure 3.5: The $\mathcal{F}.\mathcal{O}.\mathcal{M}.$ curve

Table 3.2: O_{NB} cut optimization.

O_{NB} cut	N_{sig}	N_{qq}	N_{BB}	FOM
0.5	16	945	45	0.503
0.6	15	707	42	0.542
0.7	14	487	38	0.509
0.8	12	268	32	0.666
0.81	12	247	31	0.676
0.82	11	231	30	0.681
0.83	11	213	29	0.690
0.84	11	196	28	0.696
0.85	10	174	27	0.711
0.86	10	155	26	0.722
0.87	10	136	25	0.738
0.88	9	120	24	0.742
0.89	9	102	23	0.751
0.9	8	85	22	0.767

We choose O_{NB} cut $= 0.87$ instead of 0.9 to keep more N_{sig}. Fig 3.6 shows some variables before and after O_{NB} cut. To suppress more $q\bar{q}$ background, we observe 2 variables de and $M_{\Lambda_{1520}}$. As in section 3.3.4, the principle of
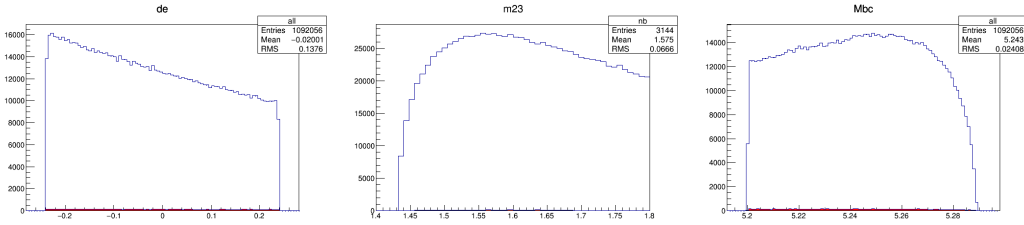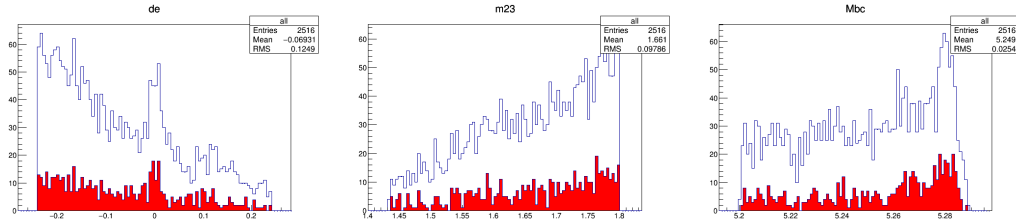
selection is to keep most signal events (up to $99\% \approx 3\sigma$). The summary of the strict selection range is showed in Table 3.3.
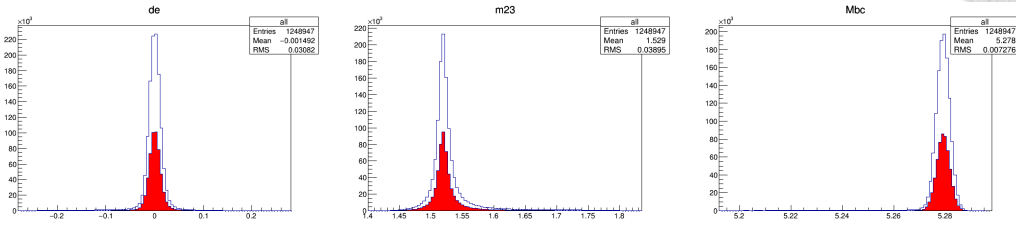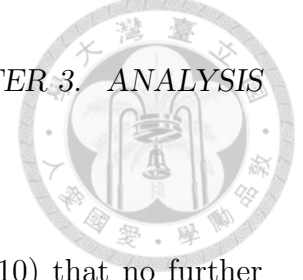

(a) signal MC

(b) $q\bar{q}$ MC

(c) generic B MC

Figure 3.6: Distributions of de, $M_{\Lambda_{1520}}$ and M_{bc}. The remained events are red-filled.(The remained are 99% Monte Carlo True for signal)

Table 3.3: Strict Selection

$O_{NB} > 0.87$
$|de| < 0.12\ GeV$
$1.45 < M_{\Lambda_{1520}} < 1.69\ GeV$

3.4.4 $B\bar{B}$ Suppression

After the strict cut, the number of $B\bar{B}$ is so small (≈ 10) that no further suppression is applied, also in order to keep the efficiency. In other words, we merge $B\bar{B}$ events with $q\bar{q}$ as "background".

We will show that $B\bar{B}$ indeed does little effect to signal extraction and ensemble test in the following section (section 3.5).

3.5 Signal Extraction

To extract signal from background, the unbinned extended likelihood fit is used, which maximizes the likelihood function:

$$\mathcal{L} = \frac{e^{-N}}{N!} \prod_{i=1}^{N} [N_{sig}P_{sig}^i(M_{bc}) + (N_{bg}P_{bg}^i(M_{bc})] \tag{3.7}$$

where i denotes the ith event, $P_{sig/bg}$ denotes the signal/background probability density function (PDF), and $N_{(sig/bg)}$ denotes the number of total (signal/background) events yield.

In this study, we use Gaussian function to describe P_{sig} and Argus function for P_{bg} for M_{bc} variable; as for de, double Gaussian function fits P_{sig} whereas 2nd-order Chebyshev polynomial function is used for P_{bg}. Fig 3.7 shows the fit result of pure signal/background events yield (5 stream of $q\bar{q}$ events). When applied to the ensemble (or real data in the future), the parameters of M_{bc} and de of signal, means and sigmas of Gaussians, are fixed (as in Fig 3.8). We will explain more for ensemble data in the next subsection.

One thing to mention is that it fits well to ensemble no matter we add $B\bar{B}$ events or not.
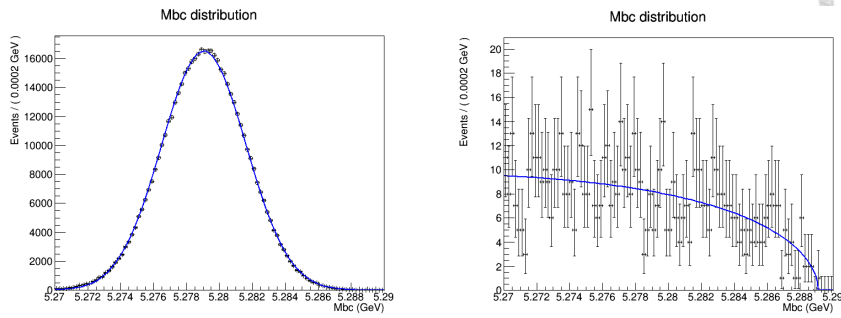
(a) M_{bc} fit for pure signal (left) and $q\bar{q}$ background (right)
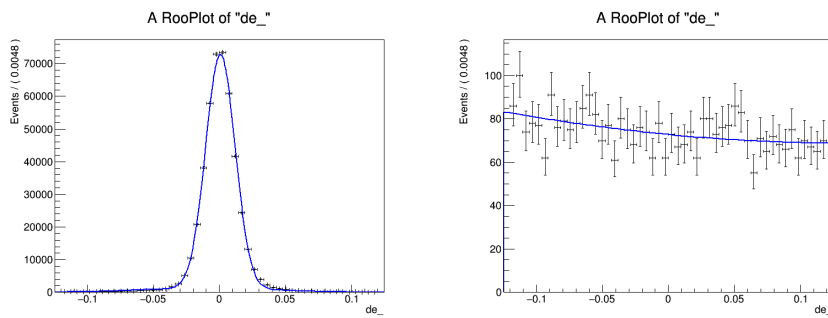
(b) de fit for pure signal (left) and $q\bar{q}$ background (right)
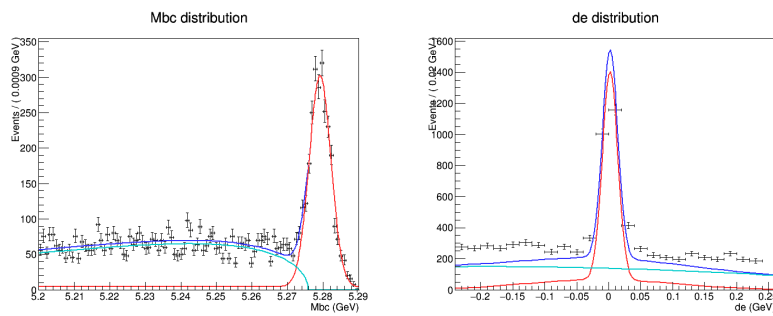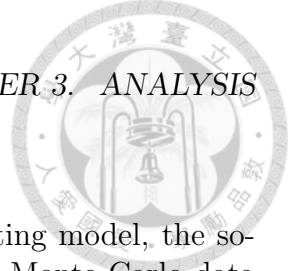
Figure 3.7: M_{bc} and de fit results by Roofit

Figure 3.8: M_{bc} and de fit results for ensemble fit by Roofit
The ensemble includes signal, $q\bar{q}$ and $B\bar{B}$.

3.5.1   Ensemble Test on Fitters

To verify the unbiasedness and stability of the above fitting model, the so-called ensemble test is applied. The model fits to plenty Monte Carlo data samples to see if the bias is small enough. In this ensemble test, 3000 MC samples are generated by mixture of Poisson-distributed numbers of signal and background, related to the expected numbers of signal and background calculated in Section 3.5.

The result is shown in Fig 3.9, where

$$Pull = \frac{Bias}{Fitting\ error} = \frac{N_{fit\ result} - N_{expected}}{Fitting\ error}. \tag{3.8}$$

According to the fitting result of the ensemble test, pull and bias are well Gaussian-distributed and almost 0-mean, thus the fitter is reliable.
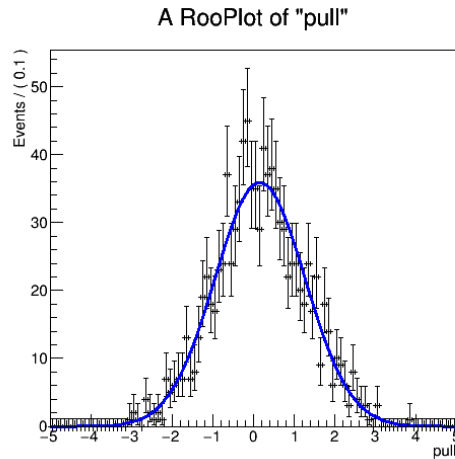

Figure 3.9: Chart of 3000 ensemble tests(Gaussian-distributed)

3.5.2   Upper Limit Estimation

Since the theoretical branching fraction of $B \to p\bar{\Lambda}_{1520}$ is too small, we can only estimate the upper limit (U.L.) of the branching fraction. The 90% confidence level (C.L.) Bayesian upper limit is calculated by the following formula:

$$\int_0^N \mathcal{L}(n)dn = 0.9 \int_0^\infty \mathcal{L}(n)dn, \qquad (3.9)$$

where $\mathcal{L}(n)$ denotes the likelihood of the fit result, given the number of signal events n. As shown in Fig 3.10, the boundary of the 90% area is $N_{sig} = 18.2$, and the corresponding branching ratio $\mathcal{B} = 5.46 \times 10^{-7}$.

With likelihood function, another method to compute the significance of signal is provided:

$$\sigma = \sqrt{-2 \times \ln \frac{\mathcal{L}_0}{\mathcal{L}_{max}}}. \qquad (3.10)$$

The calculated result is 2.565 σ, indeed a little too small to detect $B \to p\bar{\Lambda}_{1520}$ decay signal.
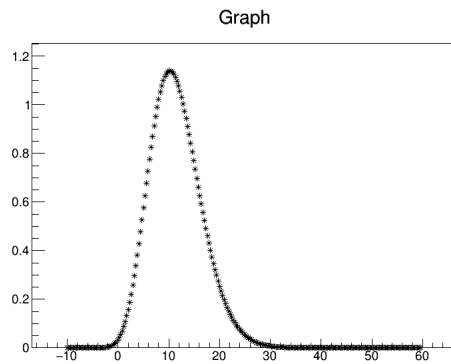

Figure 3.10: Likelihood fit result

Chapter 4

Conclusion

In conclusion, we have performed a search for the 2-body baryonic B decay $B^+ \to p\bar{\Lambda}_{1520}$ using some techniques including Monte Carlo method, NeuroBayes, likelihood fit, and etc. Although we cannot find significant signal due to lack of data in Belle, nor compare the branching fraction measured by LHCb, we still set an expected upper limit on $\mathcal{B}(B^+ \to p\bar{\Lambda}_{1520}) < 5.46 \times 10^{-7}$ at the 90% C.L.
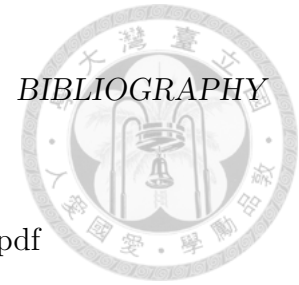
Since the KEKB accelerator and the Belle detector are now upgrading to SuperKEKB and Belle II, increasing the luminosity by a factor of 40, we are glad to see the larger integrated luminosity for a search of the decay mode, and hopefully some new physics can be found.

41

Bibliography

[1] http://en.wikipedia.org/wiki/File:Standard_Model_of_Elementary_Particles.svg

[2] M.Kobayashi and T.Maskawa,"CP-Violation in the Renormalizable Theory of Weak Interaction", Progress of Theoretical Physics 49, 2, 652-657 (1973)

[3] (Particle Data Group) http://pdg.lbl.gov/

[4] L.Wolfenstein, "Parametrization of the Kobayashi-Maskawa Matrix", Phys. Rev. Lett. 51, 1945-1947 (1983)

[5] S. W. Herb et al., "Observation of a Dimuon Resonance at 9.5 GeV in 400-GeV Proton-Nucleus Collisions", Phys. Rev. Lett. 39, 252-255 (1977)

[6] J.Beringer *et al*. (Particle Data Group), Review of Particle Physics, Phys. Rev. D 86 010001 (2012)

[7] S. Kurokawa and E. Kikutani, "Overview of the KEKB accelerators", Nucl. Instrum. Methods Phys. Res. Sect. A 499, 1, 1-7 (2003)

[8] Y. Ushiroda *et al.* (Belle Collaboration), "Development of the central trigger system for the BELLE detector at the KEK B-factory", Nucl. Instrum. Methods Phys. Res. Sect. A 438 460-471 (1999)

[9] G. Crawford *et al.*, Physics Review D Vol. 45 Num. 3 (1995)

[10] http://www2.kek.jp/accl/introKEKB/gaiyo.html

[11] A. Abashian *et al.*(Belle Collaboration), Nuclear Instruments and Methods in Physics Research A **479** 117232 (2002)

[12] http://robbep.web.cern.ch/robbep/EvtGen/GuideEvtGen.pdf

[13] http://hep.fi.infn.it/geant.pdf

[14] https://www.ifh.de/CHEP97/paper/244.ps

[15] http://osksn2.hep.sci.osaka-u.ac.jp/ taku/doc/paw.pdf

[16] https://root.cern.ch/download/doc/Users_Guide_5_26.pdf

[17] Y.-Y. Chang, M.-Z. Wang *et al.*, Phys. Rev. Lett. 115, 221803 (2015)

[18] (Belle internal page) http://belle.kek.jp/secured/wiki/doku.php?id=software:bpsmear

[19] (Belle internal page) http://belle.kek.jp/secured/wiki/doku.php?id=software:addbg

[20] M. Feindt *et al.*, Nucl.Instrum.Meth.A**654**:432-440 (2011)

[21] (Belle internal page) http://belle.kek.jp/secured/wiki/doku.php?id=software:fullreconst

[22] K.-F. Chen, T.-L. Kuo, Y.-J. Lee (Belle internal), Belle note 684 (2004)

[23] Alexei Sibidanov and Kevin Varvell (Belle internal), Belle note 1206 (2011)

[24] Bipul Bhuyan (Belle internal), Belle note 1165 (2010)

[25] Wolfgang Dungel (Belle internal) Belle note 1176 (2011)

[26] Kai-Jen Tien (Belle internal), Belle note 1279 (2012)